

## EVOLUTION OF NON-THERMAL SHELL EMISSION ASSOCIATED WITH ACTIVE GALACTIC NUCLEUS JETS

HIROTAKA ITO<sup>1</sup>, MOTOKI KINO<sup>2</sup>, NOZOMU KAWAKATU<sup>3</sup>, AND SHOICHI YAMADA<sup>4,5</sup>

<sup>1</sup> Department of Aerospace Engineering, Tohoku University, 6-6-01 Aramaki-Aza-Aoba, Aoba-ku, Sendai, 980-8579, Japan; [hito@rhd.mech.tohoku.ac.jp](mailto:hito@rhd.mech.tohoku.ac.jp)

<sup>2</sup> National Astronomical Observatory of Japan, 2-21-1 Osawa, Mitaka, Tokyo 181-8588, Japan

<sup>3</sup> Graduate School of Pure and Applied Sciences, University of Tsukuba, 1-1-1 Tennodai, Tsukuba 305-8571, Japan; [kawakatu@ccs.tsukuba.ac.jp](mailto:kawakatu@ccs.tsukuba.ac.jp)

<sup>4</sup> Science and Engineering, Waseda University, 3-4-1 Okubo, Shinjuku, Tokyo 169-8555, Japan

<sup>5</sup> Advanced Research Institute for Science & Engineering, Waseda University, 3-4-1 Okubo, Shinjuku, Tokyo 169-8555, Japan

Received 2009 November 23; accepted 2011 January 11; published 2011 March 11

### ABSTRACT

We explore the evolution of emissions by accelerated electrons in shocked shells driven by jets in active galactic nuclei. Focusing on powerful sources which host luminous quasars, we evaluated the broadband emission spectra by properly taking into account adiabatic and radiative cooling effects on the electron distribution. The synchrotron radiation and inverse Compton (IC) scattering of various photons that are mainly produced in the accretion disk and dusty torus are considered as radiation processes. We show that the resultant radiation is dominated by the IC emission for compact sources ( $\lesssim 10$  kpc), whereas the synchrotron radiation is more important for larger sources. We also compare shell emissions with those expected from the lobe under the assumption that the fractions of the energy deposited in the shell and lobe carried by non-thermal electrons are  $\epsilon_e \sim 0.01$  and  $\epsilon_{e,\text{lobe}} \sim 1$ , respectively. We find that shell emissions are brighter than lobe ones at infrared and optical bands when the source size is  $\gtrsim 10$  kpc, and the IC emissions from the shell at  $\gtrsim 10$  GeV can be observed with an absence of contamination from the lobe irrespective of the source size. In particular, it is predicted that, for most powerful nearby sources ( $L_j \sim 10^{47}$  erg s<sup>-1</sup>),  $\sim$ TeV gamma-rays produced via IC emissions can be detected by modern Cherenkov telescopes such as MAGIC, HESS, and VERITAS.

**Key words:** acceleration of particles – galaxies: active – galaxies: jets – radiation mechanisms: non-thermal – shock waves

*Online-only material:* color figure

### 1. INTRODUCTION

It is well established that radio-loud active galactic nuclei (AGNs) are accompanied by relativistic jets (e.g., Begelman et al. 1984, for review). These jets dissipate their kinetic energy via interactions with a surrounding interstellar medium (ISM) or intracluster medium (ICM), and inflate a bubble composed of decelerated jet matter, which is often referred to as a cocoon. Initially, the cocoon is highly overpressured against the ambient ISM/ICM (Begelman & Cioffi 1989) and a strong shock is driven into the ambient matter. Then a thin shell is formed around the cocoon by the compressed ambient medium. The thin-shell structure persists until the cocoon pressure decreases and the pressure equilibrium is eventually achieved (Reynolds et al. 2001).

While a large number of radio observations identified cocoons with the extended radio lobe, no clear evidence of radio emissions is found for the shocked shells (e.g., Carilli et al. 1988). Due to the lack of detections in previous studies on extragalactic radio sources, it is usually assumed that non-thermal emissions are dominated by or originated only in the cocoon (e.g., Stawarz et al. 2008). However, since strong shocks are driven into tenuous ambient gas with a high Mach number, shocked shells are expected to offer a site of particle acceleration as in the shocks of supernova remnants (SNRs), and therefore give rise to non-thermal emissions (Fujita et al. 2007; Berezhko 2008). Hence, although radio observations seem to be unsuccessful, non-thermal emissions from the shell may be accessible at higher frequencies. In fact, a recent deep X-ray observation has reported the presence of non-thermal emissions from the shell associated with the radio galaxy Centaurus A (Croston et al. 2009).

Theoretically, only a few studies have focused on non-thermal emissions from the shell. Focusing on the extended sources of  $\sim 100$  kpc, Fujita et al. (2007) evaluated emissions by accelerated electrons as well as protons in the shocked shell by approximating the dynamics of the shell as an instant explosion with fixed energy. Recently, Bordas et al. (2011) evaluated the evolution of the emissions from the shell and cocoon based on the results of hydrodynamical simulations performed in Perucho & Martín (2007). Since these studies were done in the context of FRI radio galaxies which host low luminosity nuclei in their cores, inverse Compton (IC) scattering of the photons from the core was not included in the radiative process. However, for powerful FRII radio galaxies which host luminous quasars in their cores, IC scattering of these photons can become prominent. Motivated by this background research, in this paper we focus on powerful radio sources and explore the temporal evolution of non-thermal emissions by the accelerated electrons in shocked shells, properly taking into account the Comptonization of photons of various origins. We show that the shell can produce prominent emissions ranging from radio up to  $\sim 10$  TeV gamma-ray and discuss the possibility for detecting these emissions.

This paper is organized as follows. In Section 2, we introduce our dynamical model, which describes the evolution of shell expansion, and we explain how the energy distribution of electrons residing in the shell and the spectra of the radiations they produce are evaluated based on the dynamical model. The obtained results are presented in Section 3. In Section 4, we compare the emissions from the shell with those from the lobe and discuss their detectability. We close the paper with a summary in Section 5.

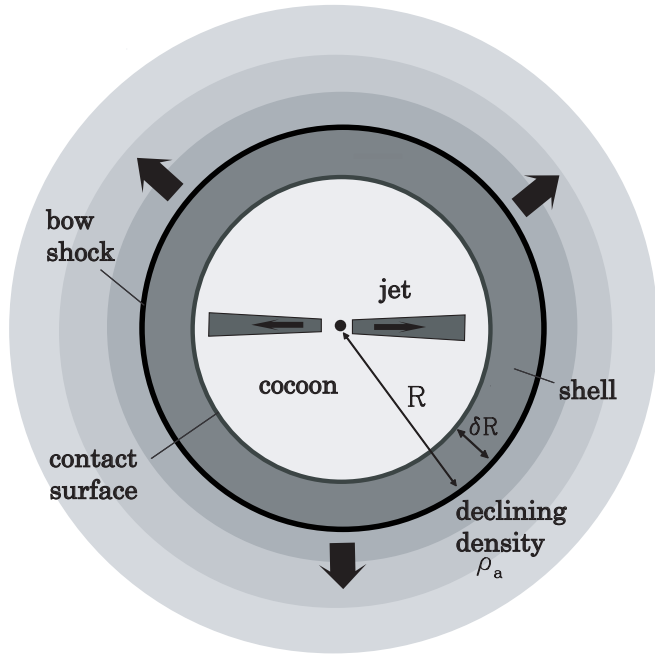


**Figure 1.** Schematic picture of the model employed in this study to approximate the expansion of the cocoon and shell produced by the jet pushing into the ambient medium from an AGN.

## 2. MODEL FOR SHELL EMISSIONS

### 2.1. Dynamics

In this section, we present a model to approximately describe the dynamics of the expanding cocoon and shell and to provide a basis on which the energy distribution of accelerated electrons and the radiation spectra are estimated. The schematic picture of the model is illustrated in Figure 1. For simplicity, we neglect the elongation of the cocoon and shell in the jet direction and assume that they are spherical. We also assume that the shell width,  $\delta R$ , is thin compared with the size of the whole system,  $R$ , and ignore the difference between the radii of the bow shock and the contact surface. This assumption is valid as long as the expansion velocity has a high Mach number (see, e.g., Ostriker & McKee 1988). We further assume that the kinetic power of the jet,  $L_j$ , is constant in time on the time scale of relevance in this study.

Under the above assumptions, the dynamics of the expanding cocoon and the shell can be approximately described by the model of stellar wind bubbles (Castor et al. 1975). The basic equations are the following: (1) the equation for the momentum of the swept-up matter in the shell and (2) the equation for the energy in the cocoon. They are expressed, respectively, as

$$\frac{d}{dt} (M_s(t) \dot{R}(t)) = 4\pi R(t)^2 P_c(t) \quad (1)$$

and

$$\frac{d}{dt} \left( \frac{P_c(t) V_c(t)}{\hat{\gamma}_c - 1} \right) + P_c(t) \frac{dV_c(t)}{dt} = L_j, \quad (2)$$

where  $\dot{R} = dR/dt$ ,  $V_c = 4\pi R^3/3$ , and  $P_c$  are the expansion velocity of the shell, and the volume and pressure of the cocoon, respectively, and  $\hat{\gamma}_c$  is the specific heat ratio for the plasma inside the cocoon. The swept-up mass in the shell is defined as  $M_s = \int_0^R 4\pi r^2 \rho_a(r) dr$  with the mass density of the ambient medium,  $\rho_a$ .

In this study,  $\rho_a$  is assumed to be given by  $\rho_a(r) = \rho_0(r/r_0)^{-\alpha}$ , with  $r_0$  and  $\rho_0$  being the reference position and the mass density, respectively. Then Equations (1) and (2) can be solved analytically and the solution is given as

$$R(t) = C_R r_0^{\alpha/(\alpha-5)} \left( \frac{L_j}{\rho_0} \right)^{1/(5-\alpha)} t^{3/(5-\alpha)}, \quad (3)$$

where  $C_R$  is a function of  $\alpha$  and  $\hat{\gamma}_c$  is given as

$$C_R = \left[ \frac{(3-\alpha)(5-\alpha)^3(\hat{\gamma}_c - 1)}{4\pi \{2\alpha^2 + (1-18\hat{\gamma}_c)\alpha + 63\hat{\gamma}_c - 28\}} \right]^{1/(5-\alpha)}.$$

Employing the non-relativistic Rankine-Hugoniot condition in the strong shock limit (Landau & Lifshitz 1959), which is justified by the assumption that the shell expands with a high Mach number, we obtain from Equation (3) the density,  $\rho_s$ , and pressure,  $P_s$ , in the shell, which are assumed to be uniform, as follows:

$$\begin{aligned} \rho_s(t) &= \frac{\hat{\gamma}_a + 1}{\hat{\gamma}_a - 1} \rho_0 \left( \frac{R(t)}{r_0} \right)^{-\alpha}, \\ P_s(t) &= \frac{2}{\hat{\gamma}_a + 1} \rho_0 \left( \frac{R(t)}{r_0} \right)^{-\alpha} \dot{R}(t)^2, \end{aligned} \quad (4)$$

where  $\hat{\gamma}_a$  is the specific heat ratio for the ambient medium. By equating  $M_s$  with the mass in the shell given by  $V_s \rho_s$ , where  $V_s = 4\pi R^2 \delta R$  is the volume of the shell, the shell width is obtained as  $\delta R = (\hat{\gamma}_a - 1)[(\hat{\gamma}_a + 1)(3 - \alpha)]^{-1} R$ . It is found that the ratio of  $\delta R$  to  $R$  does not depend on time, and the thin-shell approximation is reasonably good for typical values,  $\hat{\gamma}_a = 5/3$  and  $0 \leq \alpha \leq 2$ .

The total internal energy stored in the shell,  $E_s = P_s V_s / (\hat{\gamma}_a - 1)$ , is one of the most important quantities since it determines the energy budget for the radiation. From Equations (3) and (4),  $E_s$  can be expressed as

$$E_s = f L_j t, \quad (5)$$

where  $f$  is a fraction of the total energy released by the jet ( $L_j t$ ), which is converted to the internal energy of the shell and is given by

$$f = \frac{18(\hat{\gamma}_c - 1)(5 - \alpha)}{(\hat{\gamma}_a + 1)^2 [2\alpha^2 + (1 - 18\hat{\gamma}_c)\alpha + 63\hat{\gamma}_c - 28]}, \quad (6)$$

which turns out to be time-independent. For typical numbers,  $\hat{\gamma}_c = 4/3$ ,  $\hat{\gamma}_a = 5/3$ ,  $0 \leq \alpha \leq 2$ ,  $f$  depends on  $\alpha$  only weakly and  $f \sim 0.1$ .

### 2.2. Energy Distribution of Electrons

Assuming that a fraction,  $\epsilon_e$ , of the energy deposited in the shell,  $E_s$ , goes to the non-thermal electrons, we evaluate their energy distribution. We solve the kinetic equation governing the temporal evolution of the energy distribution of electrons,  $N(\gamma_e, t)$ , which is given as

$$\frac{\partial N(\gamma_e, t)}{\partial t} = \frac{\partial}{\partial \gamma_e} [\dot{\gamma}_{\text{cool}}(\gamma_e) N(\gamma_e, t)] + Q(\gamma_e), \quad (7)$$

where  $\dot{\gamma}_e$ ,  $\dot{\gamma}_{\text{cool}}(\gamma_e) = -d\gamma_e/dt$ , and  $Q(\gamma_e)$  are the Lorentz factor, the cooling rate via adiabatic expansions and radiative losses, and the injection rate of non-thermal electrons, respectively. The

latter two, that is, the injection rate  $Q(\gamma_e)$  and the cooling rate  $\dot{\gamma}_{\text{cool}}$ , which will be described in detail below, are evaluated based on the dynamical model described in the previous section.

Following the theory of diffusive shock acceleration (DSA; Bell 1978; Drury 1983; Blandford & Eichler 1987), we assume that non-thermal electrons are injected into the post-shock region with a power-law energy distribution of the form

$$Q(\gamma_e) = K \gamma_e^{-p} \quad \text{for } \gamma_{\min} \leq \gamma_e \leq \gamma_{\max}, \quad (8)$$

where  $\gamma_{\min}$  and  $\gamma_{\max}$  correspond to the minimum and maximum Lorentz factors, respectively. In this study, we set  $\gamma_{\min} = 1$  and the power-law index,  $p$ , is fixed at two, an appropriate value for the linear DSA in the strong shock limit. The maximum Lorentz factor is obtained by equating the cooling rate,  $\dot{\gamma}_{\text{cool}}$ , to the acceleration rate given by

$$\dot{\gamma}_{\text{accel}} = \frac{3eB\dot{R}^2}{20\xi m_e c^3}, \quad (9)$$

where  $B$  is the magnetic field strength in the shell. The so-called gyro-factor,  $\xi$ , can be identified with the ratio of the energy in ordered magnetic fields to that in turbulent ones ( $\xi = 1$  is the Bohm limit). The normalization factor,  $K$ , in the injection rate is determined from the assumption that a fraction,  $\epsilon_e$ , of the shock-dissipated energy is carried by the non-thermal electrons:  $\int_{\gamma_{\min}}^{\gamma_{\max}} (\gamma_e - 1) m_e c^2 Q(\gamma_e) d\gamma_e = \epsilon_e dE_s/dt = f \epsilon_e L_j$ . A rough estimation of the normalization factor is obtained as  $K \sim 0.1 \epsilon_e L_j / [m_e c^2 \ln(\gamma_{\max})]$ , where we used  $f \sim 0.1$  (Section 2.1). It is noted that since the factor  $K$  is proportionate to  $\epsilon_e$  and  $L_j$ , the resultant luminosity of non-thermal emissions also scales in the same manner with these quantities.

In the cooling rate,  $\dot{\gamma}_{\text{cool}}$ , both radiative and adiabatic losses are taken into account. As for the former, we consider synchrotron radiation and IC scattering of photons of various origins. The cooling rate for the adiabatic dynamical expansion is expressed for electrons with a Lorentz factor  $\gamma_e$  as

$$\dot{\gamma}_{\text{ad}} = \frac{\dot{R}}{R} \gamma_e. \quad (10)$$

The rates of the radiative coolings via synchrotron radiation and IC emissions are given, respectively, as

$$\dot{\gamma}_{\text{syn}} = \frac{4\sigma_T U_B}{3m_e c} \gamma_e^2, \quad (11)$$

and

$$\dot{\gamma}_{\text{IC}} = \frac{4\sigma_T U_{\text{ph}}}{3m_e c} \gamma_e^2 F_{\text{KN}}(\gamma_e), \quad (12)$$

where  $\sigma_T$ ,  $c$ , and  $m_e$  are the cross section of Thomson scattering, the speed of light, and the electron mass, respectively. The energy densities of magnetic fields and photons in the shell are denoted by  $U_B = B^2/8\pi$  and  $U_{\text{ph}}$ , respectively. The function  $F_{\text{KN}}(\gamma_e)$  encodes both the distributions of seed photons and the Klein–Nishina (KN) cross section for the Compton scattering and reduces to unity in the Thompson limit. Note, however, that we do not employ this limit, but calculate  $F_{\text{KN}}(\gamma_e)$  from the differential cross section for the IC scattering given in Blumenthal & Gould (1970).

The typical magnetic field strengths in elliptical galaxies and clusters of galaxies are a few  $\mu\text{G}$  (e.g., Moss & Shukurov 1996;

Vikhlinin et al. 2001; Clarke et al. 2001; Carilli & Taylor 2002; Schekochihin et al. 2005). Assuming that as it passes through a shock wave, the magnetic field is adiabatically compressed by a factor of 1–4 depending on the obliqueness of the shock to the magnetic field lines, we choose  $B = 10 \mu\text{G}$  as a fiducial value for the magnetic field strength in the shell when evaluating the acceleration rate,  $\dot{\gamma}_{\text{accel}}$ , and synchrotron cooling rate,  $\dot{\gamma}_{\text{syn}}$ . The corresponding energy density of the magnetic field is given by

$$U_B \approx 4.0 \times 10^{-12} B_{-5}^2 \text{ erg cm}^{-3}, \quad (13)$$

where  $B_{-5} = B/10 \mu\text{G}$ .

In evaluating the cooling rate for the IC scattering,  $\dot{\gamma}_{\text{IC}}$ , we take into account various seed photons of relevance in this context. In their paper, Stawarz et al. (2008) explored high-energy emissions by relativistic electrons in the radio lobes through the IC scatterings of various photons. Among them are UV emissions from the accretion disk, IR emissions from the dusty torus, stellar emissions in NIR from the host galaxy, and synchrotron emissions from the radio lobe. In addition to these emissions, we also consider the cosmic microwave background (CMB) as seed photons in this study. Following Stawarz et al. (2008), we assume that the photons from the disk, torus, host galaxy, and CMB are monochromatic and have the following single frequencies:  $\nu_{\text{UV}} = 2.4 \times 10^{15} \text{ Hz}$ ,  $\nu_{\text{IR}} = 1.0 \times 10^{13} \text{ Hz}$ ,  $\nu_{\text{NIR}} = 1.0 \times 10^{14} \text{ Hz}$ , and  $\nu_{\text{CMB}} = 1.6 \times 10^{11} \text{ Hz}$ . The photons from the radio lobe are assumed to have a continuous spectrum given by  $L_{\nu, \text{lobe}} \propto \nu^{-0.75}$ .

From the luminosity,  $L_{\text{UV}}$ , of the UV emissions by the accretion disk, the energy density of these photons in the shell is given approximately as

$$U_{\text{UV}} = \frac{L_{\text{UV}}}{4\pi R^2 c} \approx 3.0 \times 10^{-9} L_{\text{UV},46} R_1^{-2} \text{ erg cm}^{-3}, \quad (14)$$

where  $L_{\text{UV},46} = L_{\text{UV}}/10^{46} \text{ erg s}^{-1}$  and  $R_1 = R/1 \text{ kpc}$ . As is assumed in Stawarz et al. (2008), we take  $L_{\text{UV}} = 10^{46} \text{ erg s}^{-1}$  for sources with the jet kinetic power of  $L_j > 10^{45} \text{ erg s}^{-1}$ , and  $L_{\text{UV}} = 10^{45} \text{ erg s}^{-1}$  for  $L_j \leq 10^{45} \text{ erg s}^{-1}$  as fiducial values. The adopted values are appropriate for sources hosting a luminous quasar. According to the broadband observations of quasars (e.g., Elvis et al. 1994; Jiang et al. 2006), the IR and UV emissions are approximately comparable although there are some variations in the relative strengths from source to source. We hence assume that the luminosity of the IR emissions from the torus,  $L_{\text{IR}}$ , is equal to that of the UV emissions from the disk,  $L_{\text{UV}}$ , and the energy density of IR photons in the former case is estimated as

$$U_{\text{IR}} = \frac{L_{\text{IR}}}{4\pi R^2 c} \approx 3.0 \times 10^{-9} L_{\text{IR},46} R_1^{-2} \text{ erg cm}^{-3}, \quad (15)$$

where  $L_{\text{IR},46} = L_{\text{IR}}/10^{46} \text{ erg s}^{-1}$ . In evaluating the energy density of photons from the host galaxy, we assume that most of the photons are emitted by stars in the core region with the radius of  $\sim 1 \text{ kpc}$  (de Ruiter et al. 2005). Considering only the sources with  $R \gtrsim \text{kpc}$ , we can estimate the energy density of the optical photons from the luminosity,  $L_{\text{NIR}}$ , as

$$U_{\text{NIR}} = \frac{L_{\text{V}}}{4\pi R^2 c} \approx 3.0 \times 10^{-10} L_{\text{NIR},45} R_1^{-2} \text{ erg cm}^{-3}, \quad (16)$$

where  $L_{\text{NIR},45} = L_{\text{NIR}}/10^{45} \text{ erg s}^{-1}$ . The energy density of CMB photons is given by

$$U_{\text{CMB}} \approx 4.2 \times 10^{-13} \text{ erg cm}^{-3}. \quad (17)$$

The redshift is ignored for simplicity. Finally, the energy density of photons emitted from the lobe is obtained by assuming that a fraction  $\eta$  of the jet power is radiated as radio emissions from the lobe (i.e.,  $\int L_{\nu, \text{lobe}} d\nu = \eta L_j$ ). Assuming  $\eta = 10^{-2}$  as a fiducial case, it is given as

$$U_{\text{lobe}} = \frac{\int L_{\nu, \text{lobe}} d\nu}{4\pi R^2 c} \approx 3.0 \times 10^{-12} \eta_{-2} L_{45} R_1^{-2} \text{ erg cm}^{-3}, \quad (18)$$

where  $\eta_{-2} = \eta/10^{-2}$  and  $L_{45} = L_j/10^{45} \text{ erg s}^{-1}$ .

The cooling rate for the IC scattering is obtained from Equation (12) by plugging in the energy densities  $U_{\text{ph}}$  obtained above and calculating  $F_{\text{KN}}(\gamma_e)$  for the assumed photon distributions. Each contribution from the disk, torus, host galaxy, CMB, and lobe is denoted as  $\dot{\gamma}_{\text{IC,UV}}$ ,  $\dot{\gamma}_{\text{IC,IR}}$ ,  $\dot{\gamma}_{\text{IC,NIR}}$ ,  $\dot{\gamma}_{\text{IC,CMB}}$ , and  $\dot{\gamma}_{\text{IC,lobe}}$ . The total cooling rate  $\dot{\gamma}_{\text{cool}}$  is the sum of the rates for the adiabatic, synchrotron, and IC losses. ( $\dot{\gamma}_{\text{cool}} = \dot{\gamma}_{\text{ad}} + \dot{\gamma}_{\text{syn}} + \dot{\gamma}_{\text{IC,UV}} + \dot{\gamma}_{\text{IC,NIR}} + \dot{\gamma}_{\text{IC,CMB}} + \dot{\gamma}_{\text{IC,lobe}}$ ). Note that the synchrotron self-Compton is ignored, since its effect is negligible in any case considered in this study.

Now that the injection rate,  $Q(\gamma_e)$ , and the cooling rate,  $\dot{\gamma}_{\text{cool}}$ , have been evaluated, the energy distribution of non-thermal electrons,  $N(\gamma_e, t)$ , is obtained by putting these quantities in Equation (7). Although  $Q(\gamma_e)$  is time-dependent through  $\gamma_{\text{max}}$  and so is  $\dot{\gamma}_{\text{cool}}$  because of the power dependence of the expansion rate (see Equation (3)), we ignore these variations over the dynamical timescale  $\sim t$ . Then, employing the instantaneous values of  $\dot{\gamma}_{\text{cool}}(\gamma_e)$  and  $Q(\gamma_e)$  evaluated at each time and fixing them, we can solve Equation (7) by the Laplace transforms (Melrose 1980; Manolakou et al. 2007) and the solution can be written as

$$N(\gamma_e, t) = \frac{1}{\dot{\gamma}_{\text{cool}}(\gamma_e)} \int_{\gamma_e}^{\gamma_u} d\gamma'_e Q(\gamma'_e), \quad (19)$$

where the upper limit of the integral is given by

$$\gamma_u = \begin{cases} \gamma_*(\gamma_e) & \text{for } \gamma_{\text{min}} \leq \gamma_e \leq \gamma_{\text{br}} \\ \gamma_{\text{max}} & \text{for } \gamma_{\text{br}} < \gamma_e \leq \gamma_{\text{max}}. \end{cases}$$

Here,  $\gamma_*$  and  $\gamma_{\text{br}}$  are determined by the relation  $\tau(\gamma_*, \gamma_e) = \tau(\gamma_{\text{max}}, \gamma_{\text{br}}) = t$ , where the function  $\tau(\gamma', \gamma) = \int_{\gamma'}^{\gamma} d\gamma'' / \dot{\gamma}_{\text{cool}}(\gamma'')$  gives the time it takes an electron to cool from  $\gamma'$  to  $\gamma$  in the Lorentz factor. Note that  $\gamma_{\text{br}}$  corresponds to the Lorentz factor, where the energy distribution of non-thermal electrons shows a break owing to the radiative coolings (see Section 3.1 for details).

### 2.3. Radiation Spectra

From the energy distribution of non-thermal electrons just obtained, the spectrum of the synchrotron radiation is calculated as

$$L_{\nu, \text{syn}} = \int_{\gamma_{\text{min}}}^{\gamma_{\text{max}}} P_{\text{syn}}(\nu, \gamma_e) N(\gamma_e) d\gamma_e. \quad (20)$$

Here,  $P_{\text{syn}}(\nu, \gamma_e)$  is the pitch-angle-averaged power spectrum for a single electron given by

$$P_{\text{syn}}(\nu, \gamma_e) = \frac{\sqrt{3}e^3 B}{2m_e c^2} \int_0^\pi \sin^2 \theta F\left(\frac{\nu}{\nu_c}\right) d\theta,$$

where  $\theta$  is the pitch angle and  $\nu_c = 3eB\gamma_e^2 \sin \theta / 4\pi m_e c$  is the characteristic frequency of the emitted photons. The function

$F(x)$  is defined by  $F(x) = x \int_x^\infty K_{5/3}(y) dy$ , where  $K_{5/3}(y)$  is the modified Bessel function of the 5/3 order (Rybicki & Lightman 1979). Note that the synchrotron self-absorption is ignored, since it is important only at low frequencies below  $10^7 \text{ Hz}$  in the current context.

In the same way, the spectrum of the IC scattering is obtained as

$$L_{\nu, \text{IC}} = \int_{\gamma_{\text{min}}}^{\gamma_{\text{max}}} P_{\text{IC}}(\nu, \gamma_e) N(\gamma_e) d\gamma_e, \quad (21)$$

where  $P_{\text{IC}}(\nu, \gamma_e)$  is the power spectrum for a single electron in isotropic photon fields given as

$$P_{\text{IC}}(\nu, \gamma_e) = h\nu c \int_0^\infty n_{\text{ph}}(\nu_s) \sigma_{\text{IC}}(\nu, \nu_s, \gamma_e) d\nu_s.$$

Here,  $n_{\text{ph}}(\nu_s)$  and  $\sigma_{\text{IC}}(\nu, \nu_s, \gamma_e)$  are the number density of seed photons per unit frequency and the differential cross section for the IC scattering given by Blumenthal & Gould (1970), which is valid both in the Thompson and KN regimes. The origins of the seed photons have been discussed in Section 2.2. The number densities per unit frequency of these photons are then given as follows:  $n_{\text{ph}}(\nu_s) = (U_{\text{ph}}/h\nu_{\text{ph}})\delta(\nu_s - \nu_{\text{ph}})$  for the UV emissions from the accretion disk ( $U_{\text{ph}} = U_{\text{UV}}$ ,  $\nu_{\text{ph}} = \nu_{\text{UV}}$ ), the IR emissions from the torus ( $U_{\text{ph}} = U_{\text{IR}}$ ,  $\nu_{\text{ph}} = \nu_{\text{IR}}$ ), the NIR emissions from the host galaxy ( $U_{\text{ph}} = U_{\text{V}}$ ,  $\nu_{\text{ph}} = \nu_{\text{V}}$ ), and the CMB ( $U_{\text{ph}} = U_{\text{CMB}}$ ,  $\nu_{\text{ph}} = \nu_{\text{CMB}}$ );  $n_{\text{ph}}(\nu_s) = L_{\nu, \text{lobe}}/h\nu_s 4\pi R^2 c$  for the lobe emissions.

### 3. BROADBAND SPECTRUM OF THE SHELL

In the following, we focus on powerful radio sources ( $L_j \sim 10^{45} - 10^{47} \text{ erg s}^{-1}$ ) hosting luminous quasars and present the temporal evolutions of the energy distribution of non-thermal electrons and the resultant radiation spectra.

As a fiducial case, we set the parameters for the ambient matter as  $\rho_0 = 0.1 m_p \text{ cm}^{-3}$ ,  $r_0 = 1 \text{ kpc}$ , and  $\alpha = 1.5$ , i.e.,  $\rho_a(r) = 0.1 m_p \rho_{0.1} (r/1 \text{ kpc})^{-1.5} \text{ cm}^{-3}$ , where  $m_p$  is the proton mass and  $\rho_{0.1} = \rho_0/0.1 m_p$ . These are indeed typical values for elliptical galaxies (e.g., Mulchaey & Zabludoff 1998; Mathews & Brighenti 2003; Fukazawa et al. 2004, 2006). We adopt  $\hat{\gamma}_c = 4/3$  and  $\hat{\gamma}_a = 5/3$ . Then,  $R$  is given from Equation (3) as

$$R(t) \approx 22 \rho_{0.1}^{-2/7} L_{45}^{2/7} t_7^{6/7} \text{ kpc}, \quad (22)$$

where  $t_7 = t/10^7 \text{ year}$ . As mentioned in Section 2.2, the power-law index,  $p$ , for the injected non-thermal electrons (see Equation (8)) is fixed to two. Although the parameters  $\xi$  and  $\epsilon_e$  which characterize the electron acceleration efficiencies are highly uncertain, it is natural to expect that the range of these values is similar to those observed in supernova remnants (SNRs), since the nature of shocks considered here resembles those in SNRs in that they are strong non-relativistic collisionless shocks driven into the ISM. Here, we take  $\xi = 1$ , which corresponds to the Bohm diffusion limit, and  $\epsilon_e = 0.01$  as illustrative values, based on observations of SNRs (e.g., Dyer et al. 2001; Ellison et al. 2001; Bamba et al. 2003; Yamazaki et al. 2004; Stage et al. 2006; Tanaka et al. 2008). The luminosities of the emissions from the accretion disk and dust torus are taken as  $L_{\text{UV}} = L_{\text{IR}} = 10^{46} \text{ erg s}^{-1}$  for  $L_j > 10^{45} \text{ erg s}^{-1}$ , and  $L_{\text{UV}} = L_{\text{IR}} = 10^{45} \text{ erg s}^{-1}$  for  $L_j \leq 10^{45} \text{ erg s}^{-1}$ , while a fixed value of  $L_{\text{NIR}} = 10^{45} \text{ erg s}^{-1}$  is adopted for the emissions from the host galaxy. The parameters for the magnetic field and lobe emissions are chosen as  $B = 10 \mu\text{G}$  and  $\eta = 0.01$ . The employed values of the parameters are summarized in Table 1.



**Table 1**  
Model Parameters

Parameters	Symbols	Employed Values
Power-law index for density profile of ambient matter, $\rho_a(r)$	$\alpha$	1.5
Reference position in $\rho_a(r)$	$r_0$	1 kpc
Mass density, $\rho_a(r_0)$ , at $r = r_0$	$\rho_0$	$0.1 m_p \text{ cm}^{-3}$
Magnetic field strength	$B$	10 $\mu\text{G}$
Luminosity of UV emissions from accretion disk	$L_{\text{UV}}$	$10^{46} \text{ erg s}^{-1}$ (for $L_j > 10^{45} \text{ erg s}^{-1}$ ) $10^{45} \text{ erg s}^{-1}$ (for $L_j \leq 10^{45} \text{ erg s}^{-1}$ )
Luminosity of IR emissions from dust torus	$L_{\text{IR}}$	$10^{46} \text{ erg s}^{-1}$ (for $L_j > 10^{45} \text{ erg s}^{-1}$ ) $10^{45} \text{ erg s}^{-1}$ (for $L_j \leq 10^{45} \text{ erg s}^{-1}$ )
Luminosity of NIR emissions from host galaxy	$L_{\text{NIR}}$	$10^{45} \text{ erg s}^{-1}$
Ratio of lobe luminosity to jet power	$\eta$	0.01
Power-law index for energy distribution of injected electrons	$p$	2
Gyro-factor	$\xi$	1
Energy fraction of non-thermal electrons	$\epsilon_e$	0.01

### 3.1. Evolution of Non-thermal Electrons

In Figures 2 and 3, we display the cooling and acceleration timescales (left panels) and the energy distribution of non-thermal electrons (right panels). The jet powers are chosen to be  $L_j = 10^{45} \text{ erg s}^{-1}$  and  $L_j = 10^{47} \text{ erg s}^{-1}$  in Figures 2 and 3, respectively. The top, middle, and bottom panels in the figures are given for the source sizes of  $R = 1, 10$ , and 100 kpc, respectively, which in turn correspond to the different source ages. In addition to the total cooling timescale,  $t_{\text{cool}}$ , we show the contributions from the adiabatic loss,  $t_{\text{ad}} = \gamma_e / \dot{\gamma}_{\text{ad}}$ , synchrotron radiation,  $t_{\text{syn}} = \gamma_e / \dot{\gamma}_{\text{syn}}$ , and the IC scatterings of the UV disk photons,  $t_{\text{IC,UV}} = \gamma_e / \dot{\gamma}_{\text{IC,UV}}$ , IR torus photons,  $t_{\text{IC,IR}} = \gamma_e / \dot{\gamma}_{\text{IC,IR}}$ , NIR host galaxy photons,  $t_{\text{IC,NIR}} = \gamma_e / \dot{\gamma}_{\text{IC,NIR}}$ , CMB photons,  $t_{\text{IC,CMB}} = \gamma_e / \dot{\gamma}_{\text{IC,CMB}}$ , and lobe photons,  $t_{\text{IC,lobe}} = \gamma_e / \dot{\gamma}_{\text{IC,lobe}}$ , together with the source age,  $t$ .

As mentioned in Section 2.2, the Lorentz factor at the spectral break,  $\gamma_{\text{br}}$ , corresponds to the electron energy, above which cooling effects become important. It is hence determined roughly by the condition  $t \sim t_{\text{cool}}$  as shown in the left panels of Figures 2 and 3. Since the adiabatic loss is dominant over radiative coolings only below  $\gamma_{\text{br}}$ , the latter is always more important when the coolings affect the electron distribution. The relative importance of synchrotron emissions and IC emissions depends on the electron energy as well as on the energy densities of magnetic fields and photons. When the source is young and, hence, small, the energy loss is dominated by IC emissions, since the energy density of photons is larger than that of magnetic fields (referred to as the IC-dominated stage). As the source becomes larger, on the other hand, the energy density of photons decreases ( $U_{\text{ph}} \propto R^{-2}$ ) and the synchrotron loss becomes more important (the synchrotron-dominated stage). In the initial IC-dominated stage, the Lorentz factor at the break increases with the source size as  $\gamma_{\text{br}} \propto R^{5/6}$ , where we used the relations  $t \propto R^{7/6}$  and  $t_{\text{cool}} \propto \gamma_e^{-1} U_{\text{ph}}^{-1} \propto \gamma_e^{-1} R^2$ . On the other hand,  $\gamma_{\text{br}}$  decreases with source size as  $\gamma_{\text{br}} \propto R^{-7/6}$  in the synchrotron-dominated stage, since the relation  $t_{\text{cool}} \propto \gamma_e^{-1} U_{\text{B}}^{-1} \propto \gamma_e^{-1} R^0$  holds. Regarding the dependence on the jet power, for a given source size  $R$ ,  $\gamma_{\text{br}}$  increases with  $L_j$  roughly as  $\gamma_{\text{br}} \propto L_j^{1/3}$  because the dependences of the source age and the radiative cooling timescale on the jet power can be expressed as  $t \propto L_j^{-1/3}$  and  $\gamma_{\text{br}} \propto \gamma_e^{-1} L_j^0$ , respectively.

Among the contributions to the IC losses, the scattering of the IR torus photons is the largest, at least in the IC-dominated

stage, thanks to the high energy density of the IR photons. Although the UV disk photons are assumed to have the same energy density as the IR photons ( $U_{\text{UV}} = U_{\text{IR}}$ ), the cooling by the former is suppressed for  $\gamma_e \gtrsim m_e c^2 / 4h\nu_{\text{UV}} \sim 1.3 \times 10^4$  by the KN effect as seen in Figures 2 and 3. As a result, unless  $L_{\text{UV}}$  exceeds  $L_{\text{IR}}$  significantly, most electrons with  $\gamma_e \gtrsim 10^4$  cool predominantly through the IC scattering of IR photons. Then the transition from the IC-dominated stage to the synchrotron-dominated stage occurs roughly at

$$R_{\text{IC/syn}} \sim 27 L_{\text{IR,46}}^{1/2} B_{-5}^{-2} \text{ kpc}, \quad (23)$$

which corresponds to the condition  $U_{\text{IR}} \sim U_{\text{B}}$ . Since the IC scattering of IR torus photons is also suppressed by the KN effect above the Lorentz factor given by

$$\gamma_{\text{KN}} = m_e c^2 / 4h\nu_{\text{IR}} \sim 3 \times 10^6,$$

the coolings by the synchrotron emissions and/or the IC scattering of lobe photons are important at the high-energy end of non-thermal electrons ( $\gamma_{\text{KN}} \lesssim \gamma_e \lesssim \gamma_{\text{max}}$ ) for the source with  $R < R_{\text{IC/syn}}$  (see, e.g., the middle left panel of Figure 2 and the top and middle left panels of Figure 3). For even larger sources with  $R > R_{\text{IC/syn}}$ , the synchrotron emissions are the dominant cooling mechanism at all energies. The contributions from the IC scatterings of CMB and host galaxy photons, on the other hand, are modest at most during the entire evolution.

The maximum Lorentz factor of the injected electrons, which is determined by the condition  $t_{\text{cool}} = t_{\text{accel}}$  (or equivalently  $\dot{\gamma}_{\text{cool}} = \dot{\gamma}_{\text{accel}}$ ) is  $\gamma_{\text{max}} \sim 10^7$ – $10^9$  for the source sizes  $R \sim 1$ –100 kpc and the jet power  $L_j \sim 10^{45}$ – $10^{47} \text{ erg s}^{-1}$ . Regarding the dependence on the source size,  $\gamma_{\text{max}}$  increases with  $R$  for compact sources in which the cooling at  $\gamma_e \sim \gamma_{\text{max}}$  is dominated by IC emissions. This is because the cooling timescale increases rapidly with size ( $t_{\text{cool}} \propto \gamma_e^{-1} F_{\text{KN}}(\gamma_e)^{-1} U_{\text{ph}}^{-1} \propto \gamma_e^{-1} F_{\text{KN}}(\gamma_e)^{-1} R^2$ ), in contrast with the slow increase in acceleration timescale ( $t_{\text{accel}} \propto \gamma_e \dot{R}^{-2} \propto \gamma_e R^{1/3}$ ). On the other hand, for larger sources in which the cooling at  $\gamma_e \sim \gamma_{\text{max}}$  is dominated by synchrotron emissions,  $\gamma_{\text{max}}$  decreases slowly with source size ( $\gamma_{\text{max}} \propto R^{-1/6}$ ) since the cooling timescale is independent of the size ( $t_{\text{cool}} \propto \gamma_e^{-1} U_{\text{B}}^{-1} \propto \gamma_e^{-1} R^0$ ). Note that this transition takes place earlier than the transition from the IC-dominated stage to the synchrotron-dominated stage mentioned above owing to the suppression of IC emissions in high-energy electrons ( $\gamma_e \gtrsim \gamma_{\text{KN}}$ ) by the KN effect. For a given source size, higher

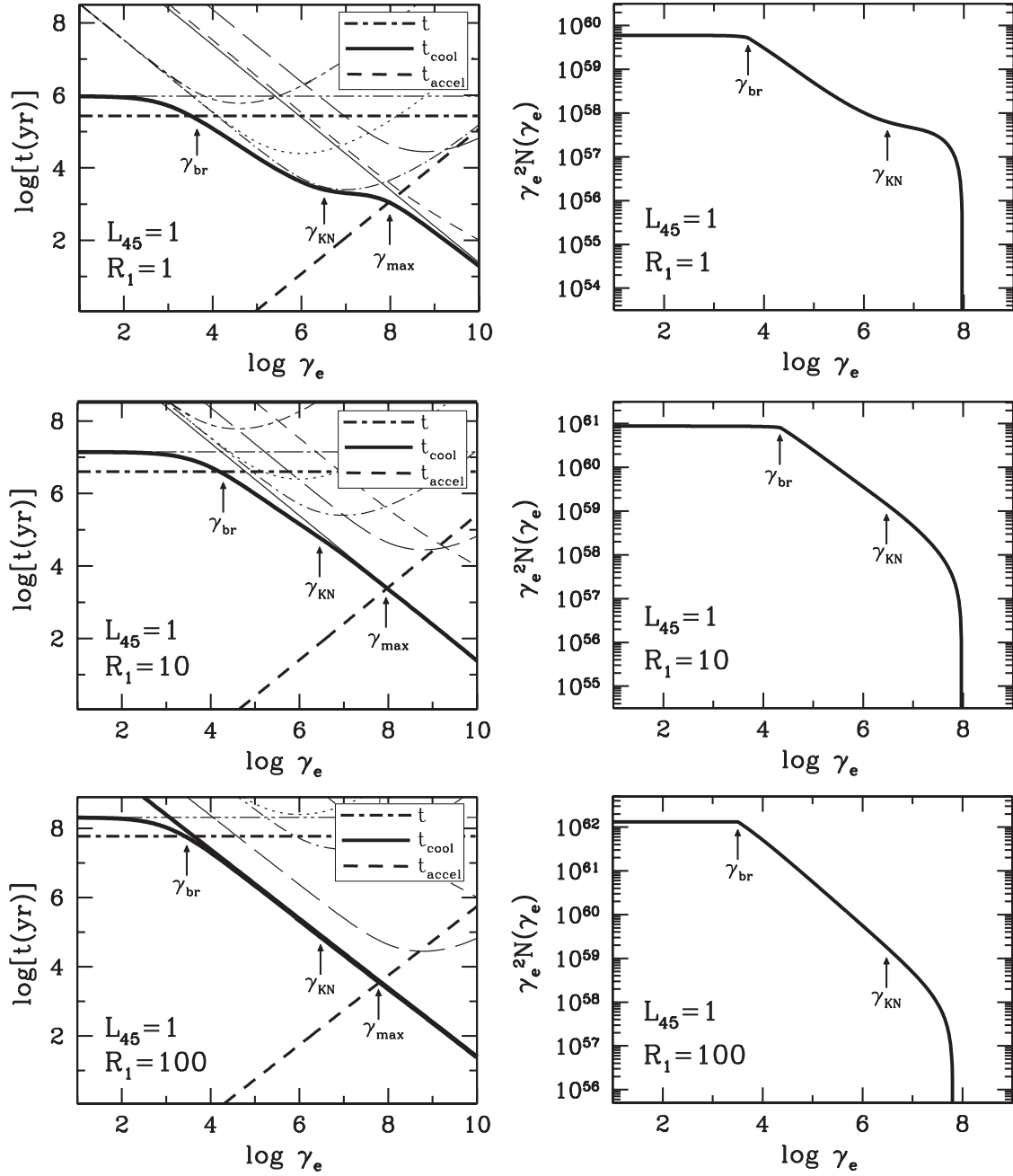


**Figure 2.** Cooling and acceleration timescales (left panels) and energy distributions of non-thermal electrons (right panels) for sources with the jet power of  $L_j = 10^{45} \text{ erg s}^{-1}$ . The top, middle, and bottom panels are shown for the source sizes of  $R = 1, 10$ , and  $100 \text{ kpc}$ , respectively. The thick lines in the left panels give the total cooling timescale (thick solid line), the acceleration timescale (thick dashed line), and the source age (thick dot-dashed line), whereas the thin lines are contributions to the total cooling timescale from various processes: adiabatic losses (dot-dot-dashed line), synchrotron emissions (thin solid line), and the IC scatterings of UV disk photons (long-short-dashed line), IR torus photons (thin dot-dashed line), NIR host galaxy photons (dotted line), lobe photons (thin short-dashed line), and CMB (thin long-dashed line) photons.

values of  $\gamma_{\text{max}}$  are obtained for sources with larger jet powers since the acceleration timescale is shorter ( $t_{\text{accel}} \propto \gamma_e L_j^{-2/3}$ ).

The resultant energy distributions of non-thermal electrons,  $N(\gamma_e)$ , are understood as follows. They have a sharp cut-off at  $\gamma_e = \gamma_{\text{max}}$ , whereas the original spectrum  $N(\gamma_e) \propto \gamma_e^{-2}$  of the injected electrons is retained at low energies below  $\gamma_{\text{br}}$ . Since the cooling effects are negligible, the energy spectrum for  $\gamma_e \lesssim \gamma_{\text{br}}$  is roughly given by  $N(\gamma_e) \sim Q(\gamma_e)t$ . The spectrum steepens for  $\gamma_e \gtrsim \gamma_{\text{br}}$  owing to the radiative cooling and is roughly determined by the energy dependence of  $t_{\text{cool}}$  as  $N(\gamma_e) \sim Q(\gamma_e)t_{\text{cool}}(\gamma_e)$ . As mentioned above, for sources

smaller than  $R_{\text{IC/syn}}$ , the IC scattering of IR torus photons determines the spectral shape up to  $\sim \gamma_{\text{KN}}$ , where the KN effect kicks in and hardens the energy spectra for higher energies (see, e.g., the top and middle panels of Figures 2 and 3). This feature is absent for larger sources ( $R > R_{\text{IC/syn}}$ ), because the synchrotron loss ( $\dot{\gamma}_{\text{syn}} \propto \gamma_e^2$ ) is dominant at all energies and the power is simply reduced by 1 ( $N(\gamma_e) \propto \gamma_e^{-3}$ ) from the original spectrum of the injected electrons. For a given source size, higher values of  $N(\gamma_e)$  are obtained for sources with larger  $L_j$ , since the electron injection rate  $Q(\gamma_e)$  is higher.

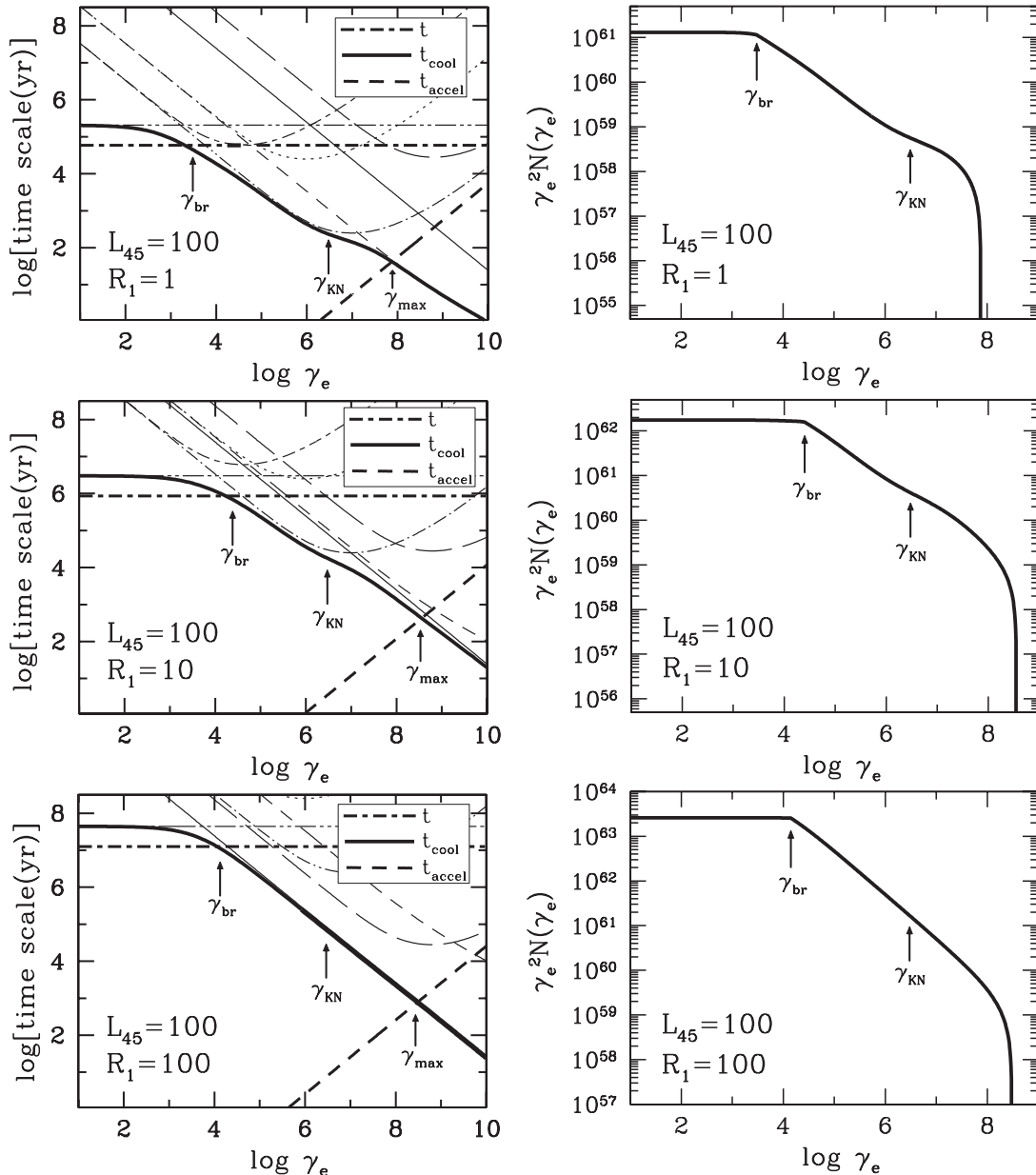


Figure 3. Same as Figure 2 but for the jet power of  $L_j = 10^{47}$  erg s $^{-1}$ .

### 3.2. Evolution of Radiation Spectra

In Figure 4, we show the radiation spectra,  $\nu L_\nu$ , which are obtained by inserting the energy distributions of non-thermal electrons in the previous section into Equations (20) and (21). It is assumed that the jet powers are  $L_j = 10^{45}$  erg s $^{-1}$  (left panels) and  $L_j = 10^{47}$  erg s $^{-1}$  (right panels). The top, middle, and bottom panels of the figure correspond to the source sizes of  $R = 1$  kpc, 10 kpc, and 100 kpc, respectively. In addition to the total luminosity (thick solid line), we show the contributions from synchrotron emissions (thin solid line) and IC scatterings of UV disk photons (long-short-dashed line), IR torus photons (dot-dashed line), NIR host galaxy photons (dotted line), CMB photons (long-dashed line), and lobe photons (short-dashed line).

The synchrotron emissions are the main low-frequency component, which extends from radio to X-ray  $\sim 2(\gamma_{max}/10^8)^2 B_{-5}$  keV. The IC emissions become remarkable at higher frequen-

cies up to gamma-ray  $\sim 50(\gamma_{max}/10^8)$  TeV. As mentioned in Section 3.1, the dominant radiative process changes from IC emissions to synchrotron radiation as the source becomes larger. As a result, the former is more luminous than the latter when the source is young and compact ( $R \lesssim R_{IC/syn}$ ) and vice versa. Owing to the hardening of the energy distributions of non-thermal electrons at  $\gamma_e \gtrsim \gamma_{KN}$  (see Figures 2 and 3) for compact sources ( $R \lesssim R_{IC/syn}$ ), their synchrotron spectrum also becomes harder than for larger sources. This feature is not so remarkable for most of the IC components mainly because the emissions themselves are suppressed by the KN effect. The IC scattering of IR dust-torus photons dominates over other IC components up to the source size of  $R \sim 85 L_{IR,46}^{1/2}$  kpc. For larger sources, on the other hand, the IC scattering of CMB photons becomes more important, since the CMB has the largest energy density of all photons considered in this paper. The contributions from the UV disk photons and NIR host galaxy photons are modest at best through the entire evolution.

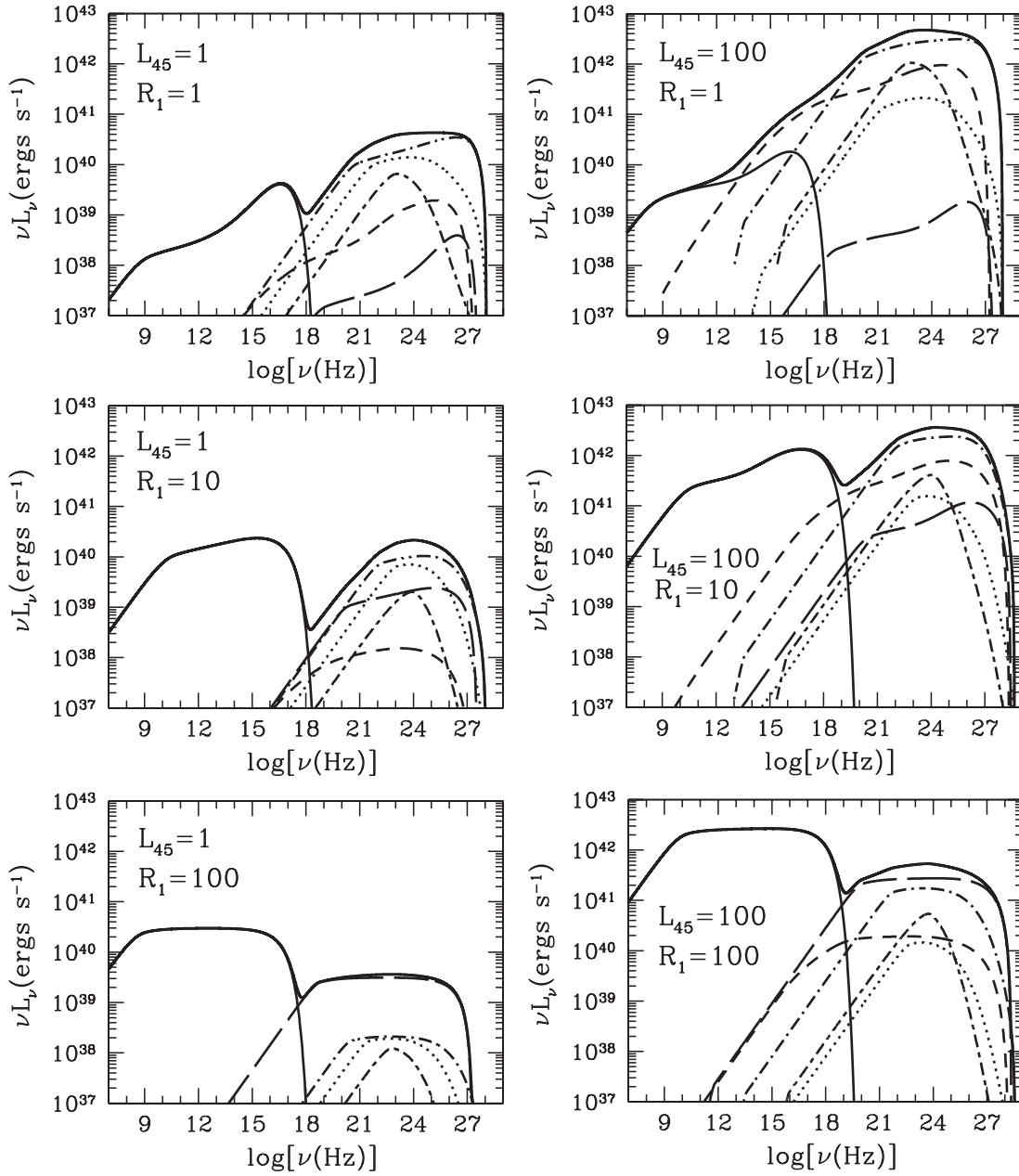


**Figure 4.** Broadband emission produced within the shell of sources with the jet powers of  $L_j = 10^{45} \text{ erg s}^{-1}$  (left panels) and  $L_j = 10^{47} \text{ erg s}^{-1}$  (right panels). The top, middle, and bottom panels are displayed for the source sizes of  $R = 1, 10$ , and  $100 \text{ kpc}$ , respectively. The various lines show the contributions from the synchrotron emissions (thin solid line) and the IC scatterings of UV disk photons (long-short-dashed line), IR torus photons (dot-dashed line), NIR host galaxy photons (dotted line), CMB photons (long-dashed line), and lobe photons (short-dashed line). The thick solid line is the sum of these emissions.

The energy injection rate above  $\gamma_{\text{br}}$  is roughly equal to the radiative output ( $\gamma_e^2 m_e c^2 Q(\gamma_e) \sim \nu L_\nu$ ) of non-thermal electrons in this energy regime because the cooling timescale is shorter than the dynamical timescale. Since the energy injection rate is independent of the electron energy ( $\gamma_e^2 Q(\gamma_e) \propto \gamma_e^0$ ), these non-thermal electrons produce a rather flat and broad spectrum ( $\nu L_\nu \propto \nu^0$ ) in the corresponding frequency range. From the relation  $\gamma_e^2 m_e c^2 Q(\gamma_e) = K m_e c^2 \sim 0.1 \epsilon_e L_j / [\ln(\gamma_{\text{max}})]$  (see Section 2.2), we can give a rough estimate to the peak luminosity as

$$(\nu L_\nu)_{\text{peak}} \sim 4.0 \times 10^{40} \epsilon_{-2} L_{45} \text{ erg s}^{-1}, \quad (24)$$

where  $\epsilon_{-2} = \epsilon_e / 0.01$ . In the above equations, we ignored the dependence of luminosity on  $\gamma_{\text{max}}$  because the luminosity only

scales logarithmically with its value, and employed a typical value  $\gamma_{\text{max}} \sim 10^8$ . The feature is clearly seen in Figure 4. Indeed, the spectra are flat with a peak luminosity given approximately by Equation (24). As mentioned in Section 2.2, the emission luminosity scales approximately linearly with the acceleration efficiency  $\epsilon_e$  and the jet power  $L_j$ . For given values of  $\epsilon_e$  and  $L_j$ , while the value of  $(\nu L_\nu)_{\text{peak}}$  remains nearly constant, the frequency range, where the spectrum is flat, varies with the source size because of the changes in  $\gamma_{\text{br}}$ ,  $\gamma_{\text{max}}$ , and the main emission mechanism (synchrotron or IC). It is emphasized that the peak luminosity is mainly governed by  $\epsilon_e$  and  $L_j$  and is quite insensitive to the magnetic field strength and seed photons, which will only affect the frequency range of the flat spectrum. This means that if  $L_j$  is constrained by other independent methods (e.g., Allen et al. 2006; Ito et al. 2008), the observation



of the peak luminosity will enable us to obtain information on the highly unknown acceleration efficiency  $\epsilon_e$ .

#### 4. COMPARISON WITH EMISSIONS FROM THE LOBE

Despite our focus on the non-thermal emission from the shell, emission from the lobe (or cocoon) is another important ingredient which arises as a consequence of the interaction of a jet with an ambient medium. As shown by Stawarz et al. (2008), lobes can produce very bright emissions in the broadband. Therefore, in order to consider the application of our model to the observation of radio sources, it is essential to investigate the relative significance of the two emissions, since the lobe component may hamper detection. In this section, we evaluate the emissions from the lobe and show the quantitative comparison between the spectra of the lobe and shell.

##### 4.1. Model for Emissions from the Lobe

We basically follow the same procedure employed for the shell in calculating the energy distribution of the electrons and the resulting emissions. Since we are considering the electrons residing in the lobe, the energy stored in the cocoon,  $E_c = P_c V_c / (\gamma_c - 1)$ , is the energy budget for the emissions. From the dynamical model described in Section 2.1, the total internal energy stored in the cocoon is given by

$$E_c = f_{\text{lobe}} L_j t, \quad (25)$$

where  $f_{\text{lobe}} = (5 - \alpha)(7 - 2\alpha)/[2\alpha^2 + (1 - 18\hat{\gamma}_c)\alpha + 63\hat{\gamma}_c - 28]$ . For  $\hat{\gamma}_c = 4/3$ ,  $\hat{\gamma}_a = 5/3$ , and  $\alpha = 1.5$ ,  $f_{\text{lobe}} = 7/13 \sim 0.5$  is obtained. As can be seen from the above equation and Equation (5),  $E_c$  is larger than  $E_s$  by a factor of  $\sim 5$ .

The energy distribution of the electrons in the lobe is determined based on Equation (7) as in the case of the shell. As described in Section 2.2, by evaluating the electron injection rate,  $Q(\gamma_e)$ , and the cooling rate,  $\dot{\gamma}_{\text{cool}}(\gamma_e)$ , the energy distribution of the electrons is obtained by putting these quantities in Equation (19) which corresponds to the solution of Equation (7). In this study, we assume that the electrons injected into the lobe have a power-law energy distribution given as

$$Q(\gamma_e) = K_{\text{lobe}} \gamma_e^{-p_{\text{lobe}}} \text{ for } \gamma_{\text{min,lobe}} \leq \gamma_e \leq \gamma_{\text{max,lobe}}. \quad (26)$$

While the employed values of the power-law index and minimum Lorentz factor are the same as those adopted for the shell ( $p_{\text{lobe}} = 2$  and  $\gamma_{\text{min,lobe}} = 1$ ), the maximum Lorentz factor is fixed as  $\gamma_{\text{max,lobe}} = 10^5$ . We will comment on the assumed value of  $\gamma_{\text{max,lobe}}$  later in Section 4.2. The normalization factor,  $K_{\text{lobe}}$ , is determined from the assumption that a fraction,  $\epsilon_{e,\text{lobe}}$ , of the energy deposited in the lobe is carried by non-thermal electrons:  $\int_{\gamma_{\text{min,lobe}}}^{\gamma_{\text{max,lobe}}} (\gamma_e - 1) m_e c^2 Q(\gamma_e) d\gamma_e = \epsilon_{e,\text{lobe}} dE_c/dt = f_{\text{lobe}} \epsilon_{e,\text{lobe}} L_j$ . A rough estimation of the normalization factor is obtained as  $K_{\text{lobe}} \sim 0.5 \epsilon_{e,\text{lobe}} L_j / [m_e c^2 \ln(\gamma_{\text{max,lobe}})]$ , where we used  $f_{\text{lobe}} \sim 0.5$ . Regarding the cooling rate of the electrons, we take into account the adiabatic losses as well as radiative losses due to synchrotron and IC emissions. The adiabatic cooling rate is evaluated from Equation (10) and coincides with that of the shell. The synchrotron cooling rate is determined from Equation (11) under the assumption that a fraction  $\epsilon_B$  of the energy  $E_c$  is carried by the magnetic fields. The corresponding energy density of the magnetic field is given as

$$U_B = \frac{\epsilon_B E_c}{V_c} \approx 4.0 \times 10^{-9} \epsilon_{B,0.1}^{1/3} L_{45}^{2/3} R_1^{-11/6} \text{ erg cm}^{-3}, \quad (27)$$

where  $\epsilon_{B,0.1} = \epsilon_B/0.1$ . As for the IC cooling rate, we take into account all seed photon fields which are considered in the shell except for the synchrotron photons from the lobe. Considering the IC of lobe photons, although a particular spectrum was assumed in the case of the shell (see Section 2.2), to be self-consistent, the distribution of the seed photons should be determined from the calculated synchrotron emissions (synchrotron self-Compton). However, the method given in Section 2.2 used to solve Equation (7) cannot be applied when a seed photon field is dependent on the electron distribution. Therefore, since the cooling rate due to the synchrotron self-Compton is modest at best in any case considered in this study, we neglected its effect merely for simplicity. As in the case of the shell, we assume that the photons from the disk, torus, host galaxy, and CMB are monochromatic with frequencies given in Section 2.2. On the other hand, while the same value is employed for the CMB, the energy densities of the disk, torus, and host galaxy photons are taken to be larger than those in the shell by a factor of three, since the lobe is located closer to the emitting sources. The cooling rate due to the IC of these photons is evaluated from Equation (12) based on the above-mentioned spectrum and energy densities.

The emission spectrum of the lobe is calculated by following the procedure described in Section 2.3. From the obtained energy distribution of the non-thermal electrons, spectra of the synchrotron and IC emission are evaluated from Equations (20) and (21), respectively. The magnetic field and seed photon fields considered above are used for the calculation. In addition, although we did not consider its contribution on the cooling rate, we also evaluate the IC of the photons from the lobe based on the calculated synchrotron spectrum.

##### 4.2. Lobe Versus Shell

For an illustrative purpose, here we examine the emissions from the lobe by assuming  $\epsilon_{e,\text{lobe}} = 1$ , an extreme case where all energy stored in the cocoon is converted to that of the non-thermal electrons, and  $\epsilon_B = 0.1$ , a magnetic field strength factor of few below the equipartition value. These values are identical to those employed in Stawarz et al. (2008). In Figure 5, we show the obtained photon fluxes,  $\nu F_\nu$ , from the lobe. In order to illustrate the comparison between the emissions from the lobe and the shell, photon fluxes from the shell are also shown in the figure. Same set of parameters which was previously assumed (Table 1) is employed for the emissions from the shell. It is assumed that the jet powers are  $L_j = 10^{45} \text{ erg s}^{-1}$  (left panels) and  $L_j = 10^{47} \text{ erg s}^{-1}$  (right panels), and the source is located at a distance of  $D = 100 \text{ Mpc}$ . The top, middle, and bottom panels of the figure correspond to the source sizes of  $R = 1 \text{ kpc}$ ,  $10 \text{ kpc}$ , and  $100 \text{ kpc}$ , respectively. We also plot the sensitivities of the *Fermi* satellite,<sup>6</sup> HESS,<sup>7</sup> and MAGIC<sup>8</sup> telescopes. The dashed and solid lines display the photon fluxes from the lobe and shell, respectively. In addition to the total photon flux (thick black line), the contributions from synchrotron emissions (thin black line) and IC scatterings of UV disk photons (blue line), IR torus photons (red line), NIR host galaxy photons (light blue line), CMB photons (green line), and lobe synchrotron photons (purple line) are also shown.

As is seen in the figure, IC emissions from the lobe tend to be brighter when the source size is smaller as in the case of the shell.

<sup>6</sup> <http://www-glast.stanford.edu>

<sup>7</sup> <http://www.mpi-hd.mpg.de/hfm/HESS>

<sup>8</sup> <http://magic.mppmu.mpg.de>

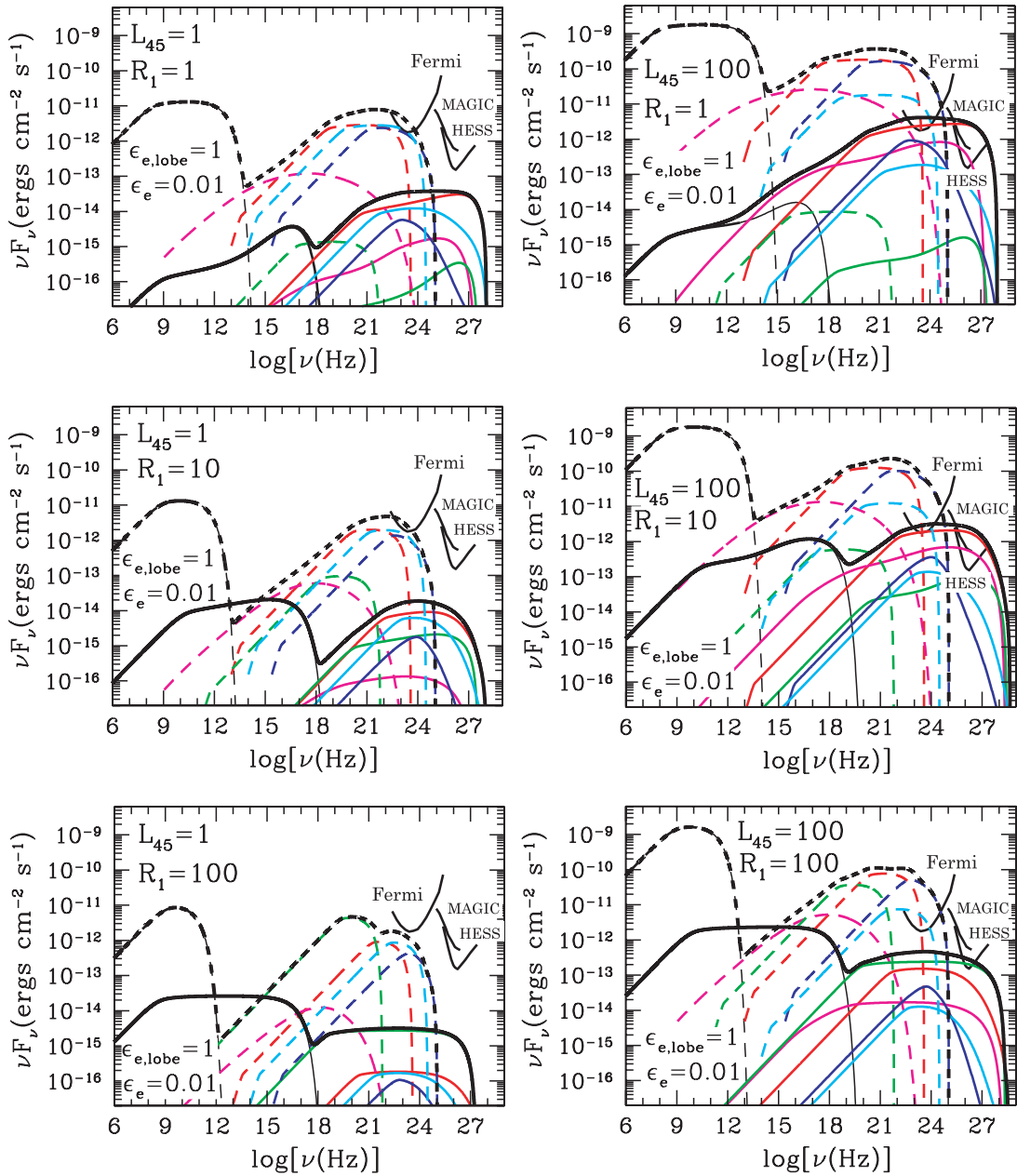


**Figure 5.** Photon fluxes from sources with the jet power of  $L_j = 10^{45} \text{ erg s}^{-1}$  (left panels) and  $L_j = 10^{47} \text{ erg s}^{-1}$  (right panels) located at the distance of  $D = 100 \text{ Mpc}$ . The top, middle, and bottom panels are displayed for the source sizes of  $R = 1, 10$ , and  $100 \text{ kpc}$ , respectively. The dashed and solid lines display the photon fluxes from the lobe and shell, respectively. The various lines show the contributions from the synchrotron emissions (thin black line) and the IC scatterings of UV disk photons (blue line), IR torus photons (red line), NIR host galaxy photons (light blue line), CMB photons (green line), and lobe synchrotron photons (purple line). The thick black lines are the sum of these fluxes. Also shown are the sensitivities of the *Fermi*, *MAGIC*, and *HESS* telescopes.

(A color version of this figure is available in the online journal.)

On the other hand, however, the emissions are synchrotron-dominated even for compact sources ( $R \sim 1\text{--}10 \text{ kpc}$ ), since the magnetic field strength is larger than that of the shell. As in the case of the shell, the luminosity scales linearly with  $\epsilon_{e,\text{lobe}}$  and  $L_j$  (see Section 2.3). A rough estimate of the peak luminosity is obtained as

$$(\nu L_\nu)_{\text{peak,lobe}} \sim 2.0 \times 10^{43} \epsilon_{e,\text{lobe}} L_{45} \text{ erg s}^{-1}. \quad (28)$$

It should be noted that the photon fluxes displayed in the figure correspond to an upper limit since  $\epsilon_{e,\text{lobe}} = 1$  is assumed.

From Equations (24) and (28), the ratio between the peak luminosities of the emissions from the lobe and shell is obtained as  $\sim 5\epsilon_{e,\text{lobe}}/\epsilon_e$ . Hence, the contrast between the two emissions

is determined by the parameters  $\epsilon_{e,\text{lobe}}$  and  $\epsilon_e$ . If  $\epsilon_{e,\text{lobe}}$  is much larger than  $\epsilon_e$ , the overall spectra are dominated by the lobe. Although there is little constraint on the values of  $\epsilon_{e,\text{lobe}}$  and  $\epsilon_e$ , it is expected that the ratio  $\epsilon_{e,\text{lobe}}/\epsilon_e$  is indeed large in most of the radio sources as is examined here due to the fact that, while a large number of radio observations identified non-thermal emissions from the lobe, no clear evidence of the shell emissions have been reported so far at the radio. It is emphasized, however, that even in the case where  $\epsilon_{e,\text{lobe}}$  is significantly larger than  $\epsilon_e$ , there are frequency ranges in which the emissions from the shell can overwhelm those from the lobe as is seen in Figure 5. This is due to the difference between the maximum energy of the electrons in the lobe and shell. Since  $\gamma_{\text{max}} \sim 10^8$  largely

exceeds  $\gamma_{\text{max,lobe}} = 10^5$ , the synchrotron and IC emissions from the shell extend up to much higher frequencies than those from the lobe, and, as a result, the shell can dominate the emission spectra at the frequencies above the cut-off frequencies of the synchrotron and IC emissions from the lobe.

Regarding synchrotron emission, although the high-frequency end of the emission is overwhelmed by the low-frequency tail of the IC emissions from the lobe, emissions from the shell can become dominant at frequencies above the cut-off frequency of synchrotron emission from the lobe which is roughly given as  $h\nu \sim 6 \times 10^{-2}(\gamma_{\text{max,lobe}}/10^5)^2 \epsilon_{\text{B},0.1}^{1/2} \rho_{0.1}^{1/6} L_{45}^{1/3} R^{-11/12}$  eV when the source size is large ( $R \gtrsim R_{\text{IC/syn}}$ ). For example, emissions from the shell can be observed at frequencies from IR to optical without strong contamination from the lobe for sources with a size of  $R \sim 100$  kpc (see the bottom panels of Figure 5). Hence, deep observations of radio galaxies at these frequencies may lead to the discovery of shell emissions. It is noted that a broader range of frequencies could be detectable if the ratio  $\epsilon_{e,\text{lobe}}/\epsilon_e$  is smaller. For compact sources ( $R \lesssim R_{\text{IC/syn}}$ ), however, synchrotron emissions are likely to be completely overwhelmed by the lobe components, since the synchrotron emissions from the shell are strongly suppressed (see the top panels of Figure 5).

On the other hand, IC emissions from the shell are not subject to the contamination from the lobe irrespective of the size of the source at frequencies above the cut-off frequency of IC emissions from the lobe, which is roughly given as  $h\nu \sim \gamma_{\text{max,lobe}} m_e c^2 \sim 50(\gamma_{\text{max,lobe}}/10^5)$  GeV, since the lobe emissions cannot extend above the frequency. It is also noted that compact sources ( $R \lesssim R_{\text{IC/syn}}$ ) are favored for detection, since the luminosity is higher. Contrary to the above argument, although the same value was assumed for the maximum Lorentz factor ( $\gamma_{\text{max,lobe}} = 10^5$ ), Stawarz et al. (2008) argued that the lobe can produce prominent emissions up to  $\sim$ TeV gamma-ray. It should be noted, however, that the emissions above the frequency  $h\nu \sim 10$  GeV in their study are considerably overestimated, since the KN effect was not taken into account. Hence, due to the absence of lobe emissions, our study demonstrates that the energy range of  $h\nu \gtrsim 10$  GeV is the most promising window for the detection of shell emissions. This can be confirmed in Figure 5. For example, while the detection of  $\sim$ GeV gamma-rays by the *Fermi* telescope may be hampered by emissions from the lobe,  $\sim$ TeV gamma-rays are accessible to the MAGIC, HESS and, although not displayed in the figure, also VERITAS gamma-ray telescopes for the most powerful source with a jet power of  $L_j = 10^{47}$  erg s $^{-1}$  located at  $D = 100$  Mpc. It is worth noting that the maximum Lorentz factor  $\gamma_{\text{max}}$  of non-thermal electrons can be constrained by the detection of a high-energy cut-off at  $h\nu \sim 50(\gamma_{\text{max}}/10^8)$  TeV in the IC emissions. Hence, observations of high-energy gamma-rays can provide us with information not only on  $\epsilon_e$  as mentioned in Section 3.2, but also on the gyrofactor  $\xi$ .

Lastly, let us comment on the employed values of  $\gamma_{\text{max}}$  and  $\gamma_{\text{max,lobe}}$ . In the above discussions, we have shown that, even in the case of  $\epsilon_{e,\text{lobe}} \gg \epsilon_e$ , the high frequency part of synchrotron ( $\sim$  IR–optical) and IC emissions ( $\sim 10$  GeV–10 TeV) from the shell can overwhelm lobe emissions. The above argument will be valid as long as (1)  $\gamma_{\text{max}} \gtrsim 10^7$  and (2)  $\gamma_{\text{max,lobe}} \lesssim 10^5$  are satisfied. Condition (1) holds if the acceleration at the shell takes place in nearly the Bohm limit ( $\xi \sim 1$ ) as shown in Figures 2 and 3. As mentioned in Section 3, since the property of the shock considered here is similar to those of SNRs in which electron acceleration at nearly Bohm diffusion is inferred

(e.g., Yamazaki et al. 2004; Stage et al. 2006; Tanaka et al. 2008), it is natural to expect that this is also the case for the shell. In fact,  $\xi \sim 1$  is inferred in the shell associated with radio galaxy Centaurus A from the X-ray observations (Croston et al. 2009). Hence, we expect that condition (1) is satisfied for the sources we focus on here. Regarding the value of  $\gamma_{\text{max,lobe}}$ , multi-wavelength studies of powerful FR II radio galaxies show that the maximum Lorentz factor of electrons residing in the lobe does not extend well beyond  $\sim 10^5$  (Stawarz et al. 2007; Godfrey et al. 2009; Yaji et al. 2010).<sup>9</sup> Although the detail of the acceleration process is highly uncertain, if this feature is also common in compact sources ( $R \sim 1$ –10 kpc), condition (2) is likely to be satisfied irrespective of the source size. It is worth noting that the recent study by Ostorero et al. (2010) has shown that the broadband spectra in some compact radio sources can indeed be fitted under the assumption of  $\gamma_{\text{max,lobe}} \sim 10^5$ .

## 5. SUMMARY

We have explored the temporal evolution of the emissions by accelerated electrons in the shocked shell produced by AGN jets. Focusing on powerful sources which host luminous quasars, we have calculated the spectra of synchrotron emission as well as the IC scatterings of various photons that will be relevant in this context. We have used a simple analytic model that describes the dynamics of the expanding shell and estimated the energy distribution of non-thermal electrons based on this model, properly taking into account both the adiabatic and radiative coolings. Below we summarize our main findings in this study.

1. When the source is small ( $R \lesssim R_{\text{IC/syn}} \sim 27 L_{\text{IR},46}^{1/2} B_{-5}^{-2}$  kpc), the dominant radiative process is the IC scattering of IR photons emitted from the dust torus. For larger sources, on the other hand, synchrotron emissions dominate IC emissions, since the energy density of photons becomes smaller than that of magnetic fields ( $U_B > U_{\text{ph}} \propto R^{-2}$ ). Through the entire evolution, the spectrum is rather broad and flat, and the peak luminosity is approximately given by  $(\nu L_\nu)_{\text{peak}} \sim 4.0 \times 10^{40} \epsilon_{-2} L_{45}$  erg s $^{-1}$ , since it is roughly equal to the energy injection rate, which is in turn determined by the jet power  $L_j$  and acceleration efficiency  $\epsilon_e$ .
2. The broadband spectra extend from the radio up to  $\sim 10$  TeV in gamma-ray for a wide range of source size ( $R \sim 1$ –100 kpc) and jet power ( $L_j \sim 10^{45}$ – $10^{47}$  erg s $^{-1}$ ). By comparing the emissions with those from the lobe, we find that the synchrotron emissions at IR and optical frequencies can be observed without being hampered by the lobe emissions for extended sources ( $R \gtrsim R_{\text{IC/syn}}$ ), while the IC emissions at  $h\nu \gtrsim 10$  GeV can be observed with an absence of contamination from the lobe irrespective of the source size. In particular, it is predicted that, for most powerful nearby sources ( $L_j \sim 10^{47}$  erg s $^{-1}$ ,  $D \lesssim 100$  Mpc),  $\sim$ TeV gamma-rays produced via IC emissions can be detected by modern Cherenkov telescopes such as MAGIC, HESS, and VERITAS.

We are grateful to H. Nagai and M. Tanaka for useful comments and discussions. We thank the anonymous referee for

<sup>9</sup> For “low-power” FR II radio sources with hotspots showing synchrotron emissions above optical frequencies, however, electrons may be accelerated to higher energies (Brunetti et al. 2003; Hardcastle et al. 2004).

constructive comments. This study was supported by the Program for Improvement of the Research Environment for Young Researchers from Special Coordination Funds for Promoting Science and Technology (SCF) commissioned by the Ministry of Education, Culture, Sports, Science and Technology (MEXT) of Japan. This work was partially supported by grants-in-aid for Scientific Research (17540267, 19104006, 21540281) from the Ministry of Education, Science and Culture of Japan. This work is supported in part by Ministry of Education, Culture, Sports, Science, and Technology (MEXT) Research Activity Start-up 2284007 (N.K.).

## REFERENCES

- Allen, S. W., Dunn, R. J. H., Fabian, A. C., Taylor, G. B., & Reynolds, C. S. 2006, *MNRAS*, **372**, 21
- Bamba, A., Yamazaki, R., Ueno, M., & Koyama, K. 2003, *ApJ*, **589**, 827
- Begelman, M. C., Blandford, R. D., & Rees, M. J. 1984, *Rev. Mod. Phys.*, **56**, 255
- Begelman, M. C., & Cioffi, D. F. 1989, *ApJ*, **345**, 21
- Bell, A. R. 1978, *MNRAS*, **182**, 443
- Berezhko, E. G. 2008, *ApJ*, **684**, L69
- Blandford, R. D., & Eichler, D. 1987, *Phys. Rep.*, **154**, 1
- Blumenthal, G. R., & Gould, R. J. 1970, *Rev. Mod. Phys.*, **42**, 237
- Bordas, P., Bosch-Ramon, V., & Perucho, M. 2011, *MNRAS*, **tmp**, 8
- Brunetti, G., Mack, K.-H., Prieto, M. A., & Varano, S. 2003, *MNRAS*, **345**, L40
- Carilli, C. L., Perley, R. A., & Dreher, J. H. 1988, *ApJ*, **334**, L73
- Carilli, C. L., & Taylor, G. B. 2002, *ARA&A*, **40**, 319
- Castor, J., McCray, R., & Weaver, R. 1975, *ApJ*, **200**, L107
- Clarke, T. E., Kronberg, P. P., & Böhringer, H. 2001, *ApJ*, **547**, L111
- Croston, J. H., et al. 2009, *MNRAS*, **395**, 1999
- de Ruiter, H. R., Parma, P., Capetti, A., Fanti, R., Morganti, R., & Santantonio, L. 2005, *A&A*, **439**, 487
- Drury, L. O'C. 1983, *Rep. Prog. Phys.*, **46**, 973
- Dyer, K. K., Reynolds, S. P., Borkowski, K. J., Allen, G. E., & Petre, R. 2001, *ApJ*, **551**, 439
- Ellison, D. C., Slane, P., & Gaensler, B. M. 2001, *ApJ*, **563**, 191
- Elvis, M., et al. 1994, *ApJS*, **95**, 1
- Fujita, Y., Kohri, K., Yamazaki, R., & Kino, M. 2007, *ApJ*, **663**, L61
- Fukazawa, Y., Botoya-Nonesca, J. G., Pu, J., Ohto, A., & Kawano, N. 2006, *ApJ*, **636**, 698
- Fukazawa, Y., Makishima, K., & Ohashi, T. 2004, *PASJ*, **56**, 965
- Godfrey, L. E. H., et al. 2009, *ApJ*, **695**, 707
- Hardcastle, M. J., Harris, D. E., Worrall, D. M., & Birkinshaw, M. 2004, *ApJ*, **612**, 729
- Ito, H., Kino, M., Kawakatu, N., Isobe, N., & Yamada, S. 2008, *ApJ*, **685**, 828
- Jiang, L., et al. 2006, *AJ*, **132**, 2127
- Landau, L., & Lifshitz, F. M. 1959, *Fluid Mechanics* (Oxford: Pergamon)
- Manolakou, K., Horns, D., & Kirk, J. G. 2007, *A&A*, **474**, 689
- Mathews, W. G., & Brighenti, F. 2003, *ARA&A*, **41**, 191
- Melrose, D. B. 1980, *Plasma Astrophysics: Nonthermal Processes in Diffuse Magnetized Plasmas*, Vol. 2 (New York: Gordon and Breach)
- Moss, D., & Shukurov, A. 1996, *MNRAS*, **279**, 229
- Mulchaey, J. S., & Zabludoff, A. I. 1998, *ApJ*, **496**, 73
- Ostorero, L., et al. 2010, *ApJ*, **715**, 1071
- Ostriker, J. P., & McKee, C. F. 1988, *Rev. Mod. Phys.*, **60**, 1
- Perucho, M., & Martín, J. M. 2007, *MNRAS*, **382**, 526
- Reynolds, C. S., Heinz, S., & Begelman, M. C. 2001, *ApJ*, **549**, L179
- Rybicki, G. B., & Lightman, A. P. 1979, *Radiative Processes in Astrophysics* (New York: Wiley-Interscience)
- Schekochihin, A. A., Cowley, S. C., Kulsrud, R. M., Hammett, G. W., & Sharma, P. 2005, *ApJ*, **629**, 139
- Stage, M. D., Allen, G. E., Houck, J. C., & Davis, J. E. 2006, *Nature Phys.*, **2**, 614
- Stawarz, L., Cheung, C. C., Harris, D. E., & Ostrowski, M. 2007, *ApJ*, **662**, 213
- Stawarz, L., Ostorero, L., Begelman, M. C., Moderski, R., Kataoka, J., & Wagner, S. 2008, *ApJ*, **680**, 911
- Tanaka, T., et al. 2008, *ApJ*, **685**, 988
- Vikhlinin, A., Markevitch, M., & Murray, S. S. 2001, *ApJ*, **549**, L47
- Yaji, Y., Tashiro, M. S., Isobe, N., Kino, M., Asada, K., Nagai, H., Koyama, S., & Kusunose, M. 2010, *ApJ*, **714**, 37
- Yamazaki, R., Yoshida, T., Terasawa, T., Bamba, A., & Koyama, K. 2004, *A&A*, **416**, 595